Electronic Supplementary Information

Inside-Out Regulation of MnO toward Fast Reaction Kinetics in Aqueous Zinc Ion Batteries

Zixiang Cui,[ab] Jing Zhang,[ab] Shenfei Zhao,[c] Ke Wu,[ab] Chunjie Li,[b] Ruguang Ma,*[b] and Chang Ming Li*[b]

a. *School of Physical Science and Technology, Suzhou University of Science and Technology, Suzhou 215009, China Address here.*

b. *School of Materials Science and Engineering, Suzhou University of Science and Technology, Suzhou 215009, China*

c. *Institute for Clean Energy & Advanced Materials, School of Materials & Energy, Southwest University, Chongqing, 400715, PR China*

Material synthesis

1.1 MnO: Firstly, 735 mg of $Mn(CH_3COO)_2{\cdot}4H_2O$ and 150mg of PVP were uniformly dissolved in ethanol/water (75/75mL), labeled as solution **A**. Then, 1350mg of H_3BTC was uniformly dissolved in ethanol/water (75/75mL), labeled as solution **B**. Solution **B** was slowly added dropwise to solution **A** and stirred continuously for 30 minutes to obtain solution **C**. Solution **C** was left to stand for 24 hours at 60 ℃, centrifuged, washed, and dried to obtain Mn-BTC precursor. Mn-BTC was calcined at 700 ℃ in an argon atmosphere for 3 hours at a heating rate of 5 ℃/min to obtain MnO material.

1.2 Ni-MnO: When synthesizing Mn-BTC precursor, 186.5 mg of $Ni(CH_3COO)_2{\cdot}4H_2O$ was added to solution **A**, and stirred continuously for 30 minutes to obtain solution **C**. Solution **C** was left to stand for 24 hours at 60 ℃, centrifuged, washed, and dried to obtain Ni-Mn-BTC precursor. Ni-Mn-BTC was calcined at 700 ℃ in an argon atmosphere for 3 hours at a heating rate of 5 ℃/min to obtain Ni-MnO material.

1.3 Ni-MnO@rGO: When synthesizing Mn-BTC precursor, 186.5 mg of Ni $(CH_3COO)_2{\cdot}4H_2O$ and 100 mg of GO were added to solution **A**, and stirred continuously for 30 minutes to obtain solution **C**. Solution **C** was left to stand for 24

hours at 60 ℃, centrifuged, washed, and dried to obtain Ni-Mn-BTC@GO precursor. Ni-Mn-BTC@GO was calcined at 700 ℃ in an argon atmosphere for 3 hours at a heating rate of 5 ℃/min to obtain Ni-MnO@rGO material.

Characterization

Morphological and microstructural information of the samples were obtained using a field emission scanning microscope (FESEM, JSM-IT800, Japan), and transmission electron microscope (TEM, FEI Tecnai G2 F20, America). The elemental distribution was recorded using an energy-dispersive spectrometer (EDS) connected to a TEM (Hitachi HF5000, Japan). The crystal structure information of samples was obtained by X-ray diffractometer (XRD, Bruker D8A A25, Germany) with a Cu Kα source (λ=1.5418 Å). The chemical composition and electronic structure of the samples were analyzed by X-ray photoelectron spectroscopy (XSP, Thermo Scientific ESCALAB Xi^+, America) with a monochromatic Al anode X-ray source. The elemental content of the samples was measured by an elemental analyzer (Elementar Unicube, Germany). Raman spectra were recorded by using Horiba LabRAM Evolution Laser with the wavelength of 532nm (2.33eV). The nitrogen adsorption-desorption isotherm curves of the samples were measured by Autosorb-iQ automatic specific surface and pore size distribution analyzer (Quantachrome, America). The Quenched Solid Density Functional Theory (QSDFT) mode was chosen to analyze the pore diameter, pore type, and pore volume of the samples. Thermogravimetric analysis (TGA) was carried out using a Mettler Toledo thermal analyzer at a heating rate of 5 $^oC\ min^{-1}$ in the range of 32~800 ^oC in air. Electron paramagnetic resonance (EPR) was carried out using a Bruker EMX spectrometer.

Electrochemical measurements

The active materials (MnO, N-MnO, or N-MnO@rGO), carbon black and polyvinylidene fluoride (PVDF) with the mass ratio of 7:2:1, were mixed and ground into a homogeneous slurry for 30 min in N-methyl-2-pyrrolidone (NMP). Then the slurry was coated on titanium foils utilized as the cathode, and the metallic Zn sheet

was utilized as the anode. CR2025 coin cells were assembled by adding 75 mL of 3 M Zn $(CF_3SO_3)_2$ as electrolyte and using glass fiber as separator. The cyclic voltammetry (CV) and electrochemical impedance spectroscopy (EIS) were conducted on the electrochemical station of CHI 760E. The CV curves were recorded in the potential range of 1.0 V-1.90 V vs. Zn^{2+}/Zn at a scanning rate of 0.1, 0.2, 0.4, 0.6, 0.8, and 1.0 mV s^{-1}, respectively. EIS tests were performed at the open circuit potential in a frequency range of 10 kHz to 0.1 Hz. Galvanostatic charge-discharge (GCD) and galvanostatic intermittent titration technique (GITT) were performed on LANHE CT3002A battery test systems (Wuhan, China). GCD were measured within the potential window of 1.0-1.90 V vs. Zn^{2+}/Zn. All the electrochemical tests were carried at room temperature.

DFT Calculations

DFT calculations were performed by using Vienna Ab initio Simulation Package (VASP) with the Hubbard model (DFT+U).[1,2] The value of the correlation energy (U) was fixed at 5.5 and 4.5 eV for the 3d orbitals of Ni and Mn, respectively.[3,4] Projector augmented plane wave (PAW) method was adopted. The cutoff energy of 450 eV was used to expand the plane wave basis and the generalized gradient approximation (GGA) was applied for the electron exchange correlations. The unit cell of MnO was used for calculations. For the Ni-doped MnO (Ni-MnO), Ni(1)-MnO represents Ni atom substituting the Mn atom at face center, while Ni(2)-MnO means Ni atom occupying the sites of Mn atom at the vertex. The content of Ni doping is 25% at.% (1/4) by chance, very close to the experimental composition. To achieve geometric optimization, we employed the integrations over the Brillouin zone with gamma K-points. The geometric structures of all samples were relaxed until total energy converged to 10^{-5} eV and force on each atom converged to less than 0.01 eV $Å^{-1}$.

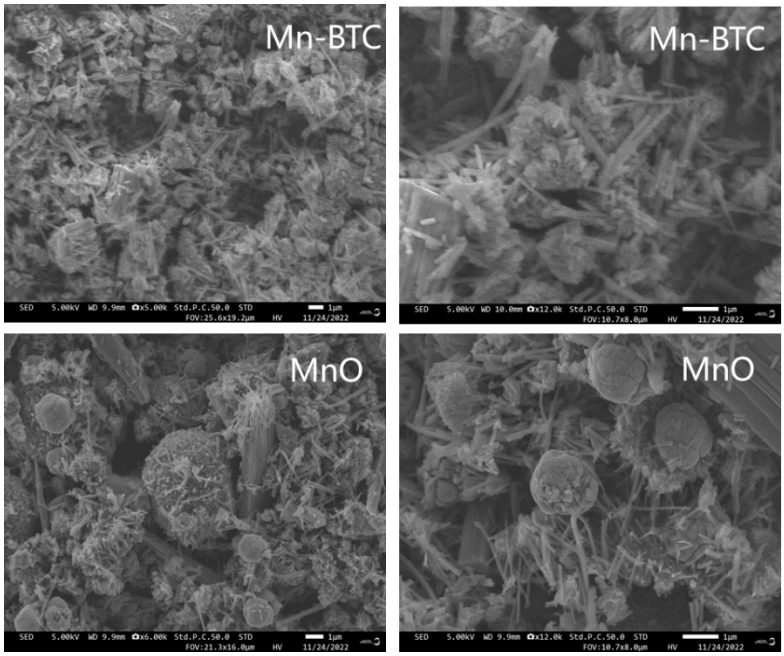

Fig. S1 SEM images of Mn-BTC and MnO, respectively.

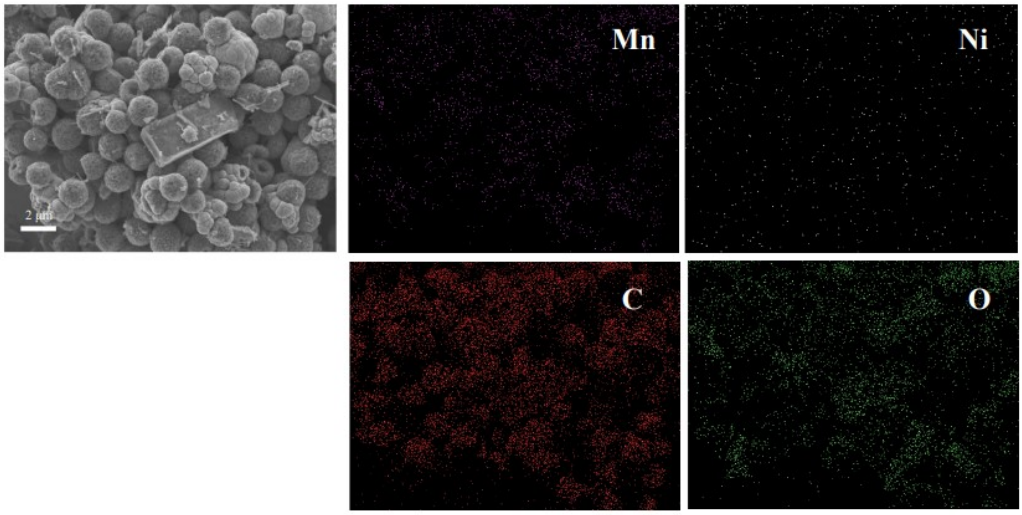

Fig. S2 SEM image and element mapping images of Ni-MnO.

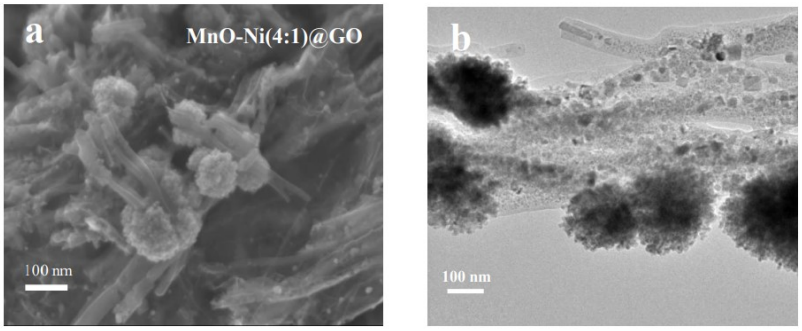

Fig. S3 (a) SEM and (b) TEM images of Ni-MnO@rGO.

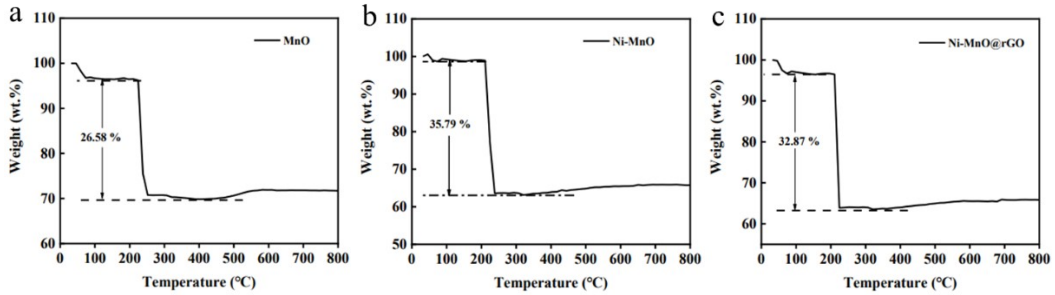

Fig. S4 Thermogravimetric analysis of MnO, Ni-MnO and Ni-MnO@rGO in O_2 atmosphere.

The carbon content in MnO or Ni-MnO is derived from the pyrolysis of Mn-BTC or Ni doped Mn-BTC. The weight loss from 100 to 300 °C can be mostly attributed to the carbon content.[5]

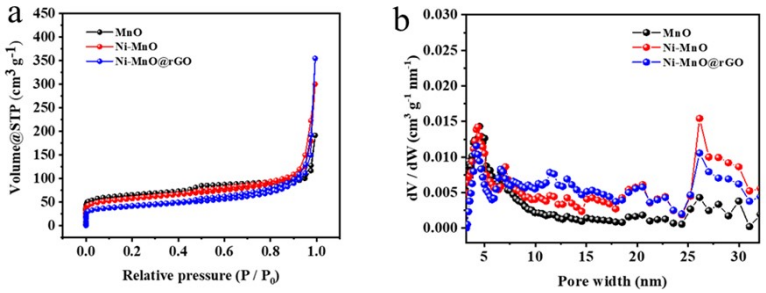

Fig. S5 Nitrogen sorption isotherms and pore size distribution of MnO, Ni-MnO and Ni-MnO@rGO.

The specific surface area (SSA) of MnO, Ni-MnO, and Ni-MnO@rGO is about146.894, 206.449 and 235.772 m^2 g^{-1} (Fig. S5a). The decrease of SSA could be caused by by the wrap of rGO, because the bare MnO has porous structure. All the three samples show mesopore characteristics as shon in Fig. S5b.

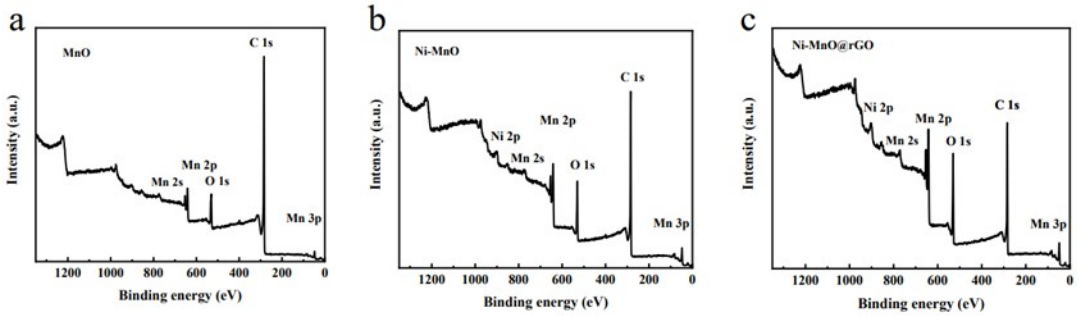

Fig. S6 XPS survey spectra of (a) MnO, (b) Ni-MnO and (c) Ni-MnO@rGO.

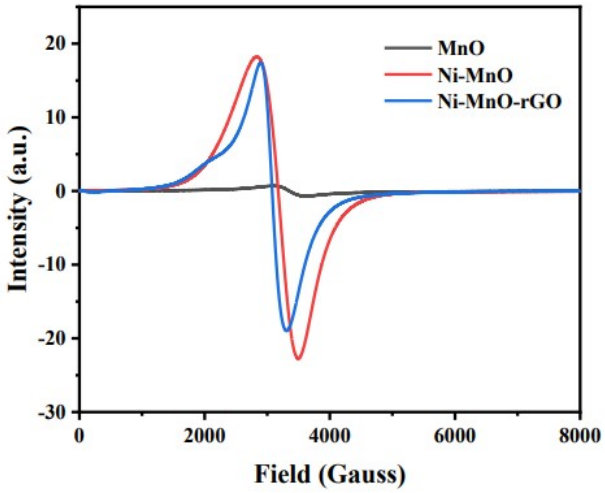

Fig. S7 EPR spectra of MnO, Ni-MnO and Ni-MnO@rGO.

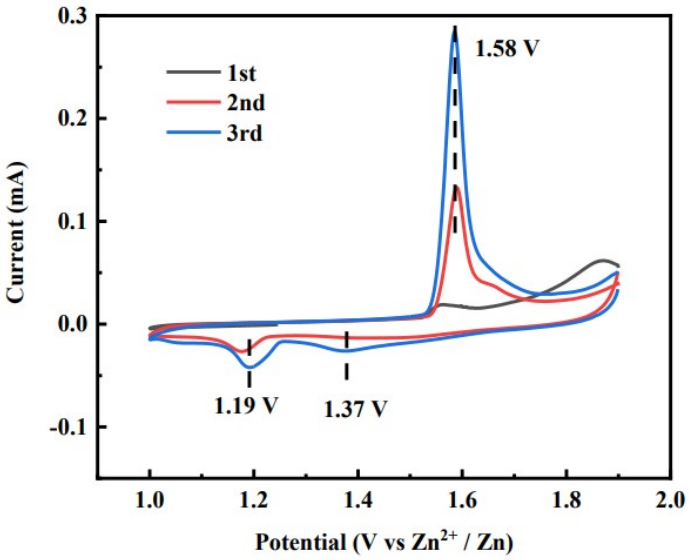

Fig. S8 CV curves of MnO at the scan rate of 0.1 mV s^{-1}.

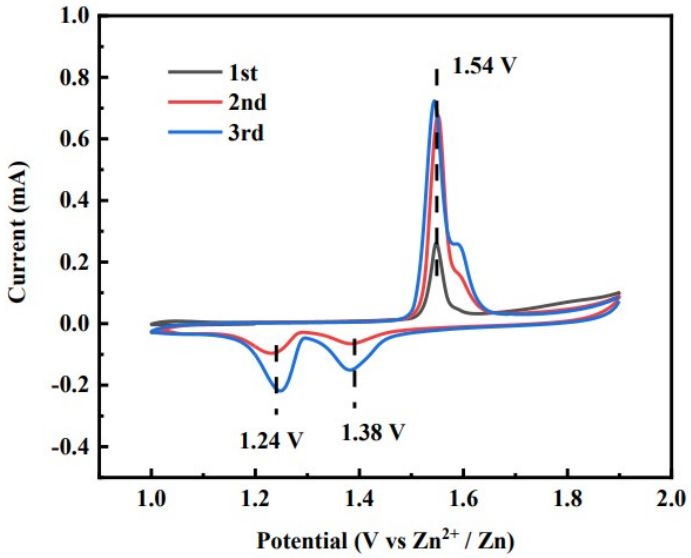

Fig. S9 CV curves of Ni-MnO at the scan rate of 0.1 mV s^{-1}.

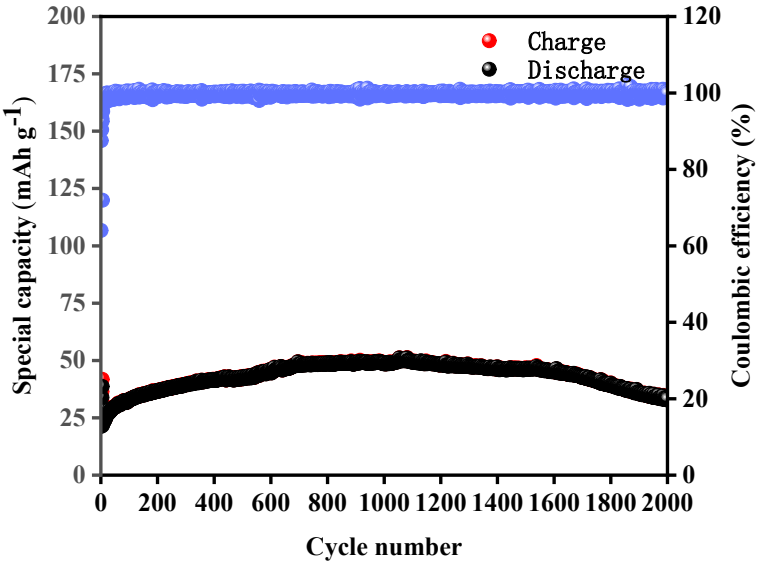

Fig. S10 Cycling performance at a current density of 2 A g^{-1} for the Ni-MnO electrodes.

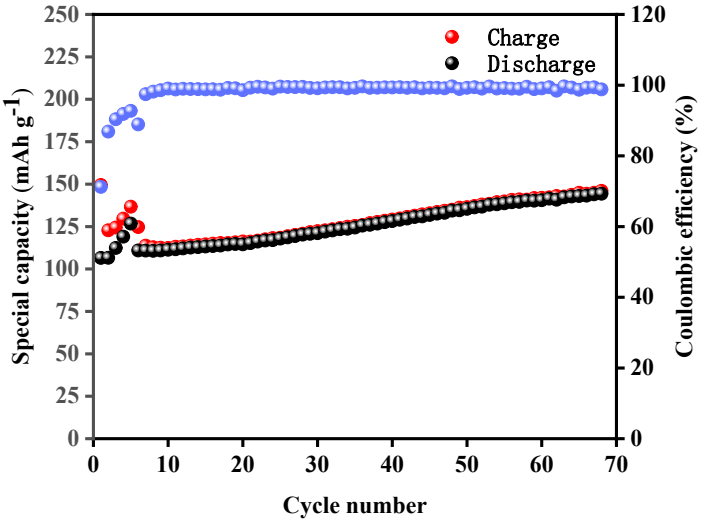

Fig. S11 Cycling performance at a current density of 0.5 A g^{-1} for the Ni-MnO@rGO electrodes.

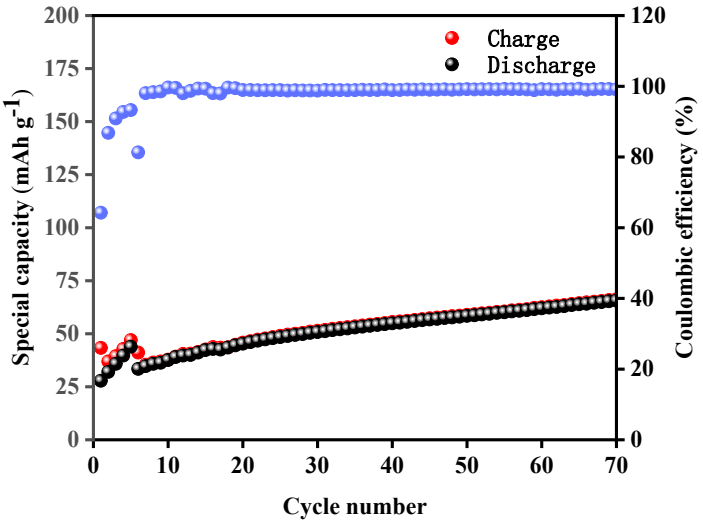

Fig. S12 Cycling performance at a current density of 0.5 A g^{-1} for the Ni-MnO electrodes.

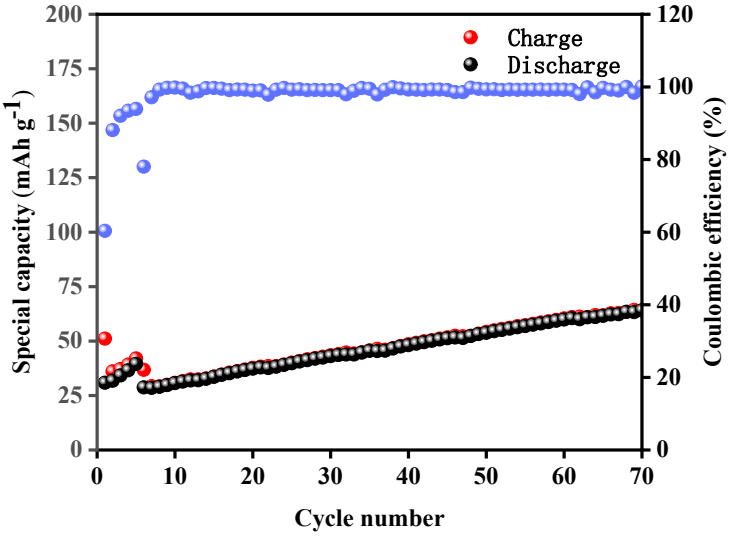

Fig. S13 Cycling performance at the current density of 0.5 A g^{-1} for the MnO electrodes.

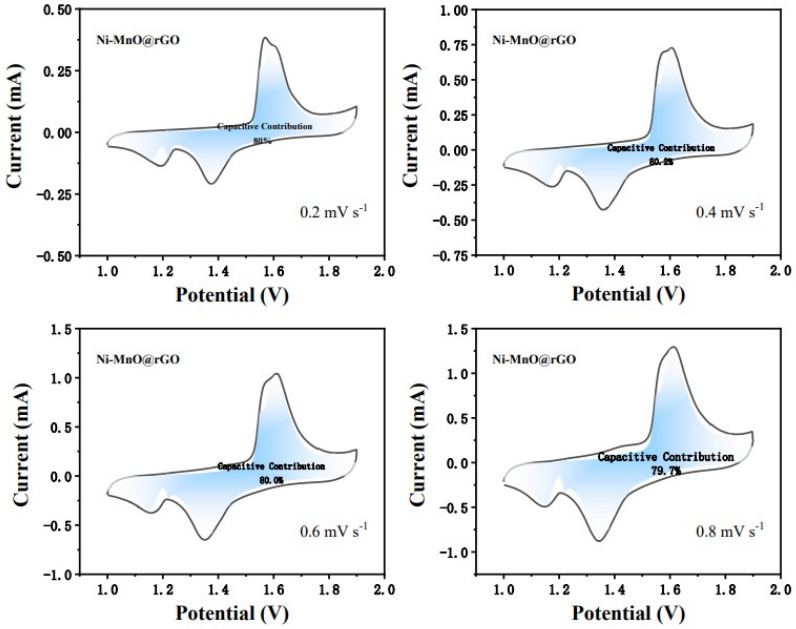

Fig. S14 Pseudocapacitance contribution of Ni-MnO@rGO at different scanning speeds.

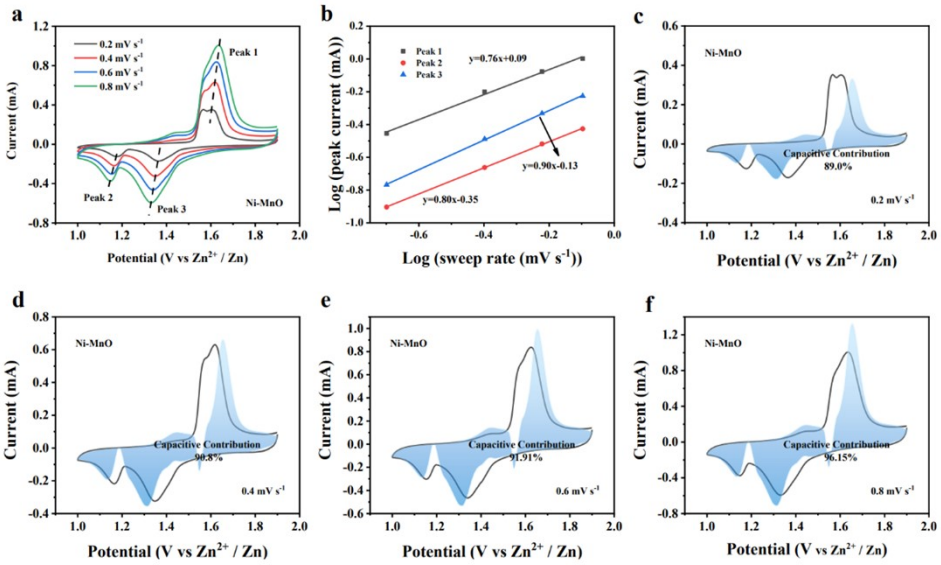

Fig. S15 (a) Ni-MnO curves measured at different scan rates from 0.2 to 0.8 mV s^{-1}; (b) *b* value according to the relationship of log(*i*) and log(*v*) at different peaks; (c-f) Pseudocapacitance contribution at different scanning speeds.

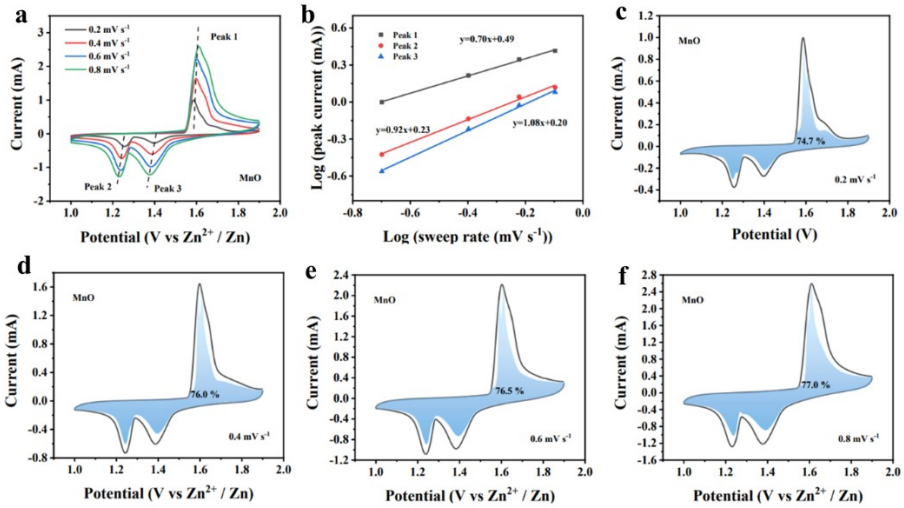

Fig. S16 (a) MnO curves measured at different scan rates from 0.2 to 0.8 mV s^{-1}; (b) *b* value according to the relationship of log(*i*) and log(*v*) at different peaks; (c-f) Pseudocapacitance contribution at different scanning speeds.

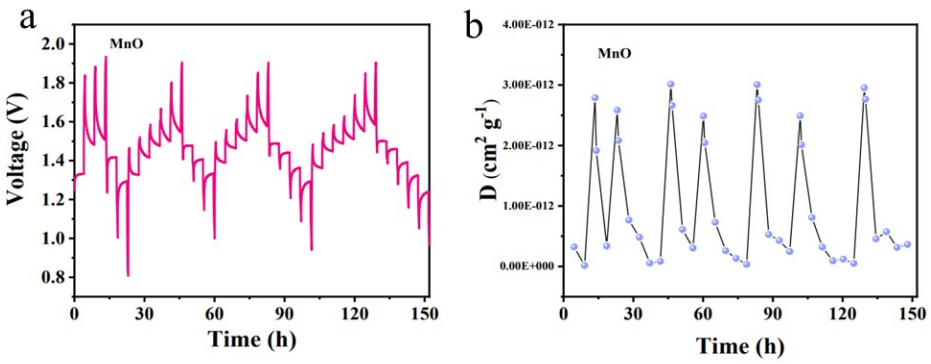

Fig. S17 (a) Charge/discharge profiles of MnO electrode in GITT test and (b) the Zn^{2+} diffusivity coefficient (10^{-13}-10^{-12} cm^2 s^{-1}).

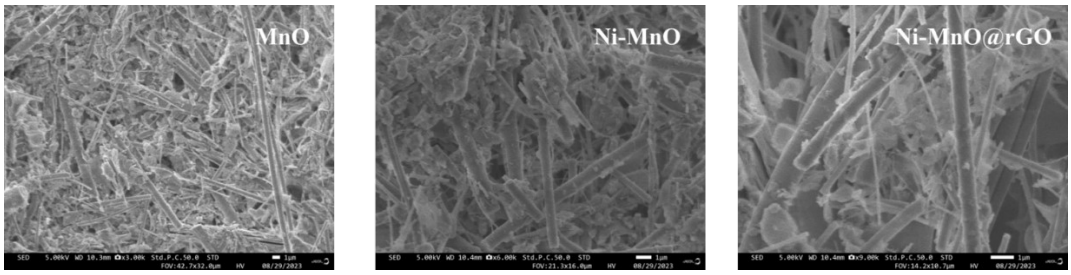

Fig. S18 SEM images of MnO, Ni-MnO and Ni-MnO@rGO after the cycling test.

The morphology of electrode materials after the cycling test was observed by SEM. Due to the strong binder, some fibers from the separator are observed. The Ni-MnO particles are still observed, especially for Ni-MnO@rGO, which suggests the good stability caused by the rGO wrap.

Table S1 Statistics of Mn-based cathode materials electrochemical measurements.

Sample	Current density (mA g^{-1})	Cycle number	Capacity retention (mAh g^{-1})	Ref.
MnO@NGS	500	300	112.308	[6]
MnO@N-C	500	200	100.5	[7]
MnOx@N-C	2000	1600	100	[8]
CNTs@Mn_3O_4	1000	500	123	[9]
D- Mn_3O_4	300	200	284	[10]
β-MnO_2@CC	100	700	326	[11]
α-MnO_2	200	1000	322	[12]
α-MnO_2/rGO	500	100	248.8	[13]
β-MnO_2	100	200	270	[14]
δ-MnO_2	100	500	335	[15]
δ-MnO_2	100	700	398.2	[16]
α-MnO_2	1000	5000	100	[17]
A-$MnO_{2-\delta}$	100	1000	301	[18]
δ-MnO_2	1200	600	280	[19]
α-MnO_2	300	3000	362.2	[20]
This work	2000	800	112	/

References

[1] Kresse, G.; Furthmüller, J. *Comp. Mater. Sci.* 1996, 6, 15-50.

[2] Kresse, G.; Furthmüller, J. *Phys. Rev. B* 1996, 54, 11169-11186.

[3] Liechtenstein, A. I.; Anisimov, V. I.; Zaanen, J. *Phys. Rev. B* 1995, 52, R5467.

[4] Tianran Zhang , Fangyi Cheng , Jing Du , Yuxiang Hu , and Jun Chen *Adv. Energy Mater.* 2015, 5, 1400654.

[5] J. Zhu, X. Zuo, X. Chen, Y. Ding, *Synthetic Met.*, 2021, 280, 116872.

[6] W. Li, X. Gao, Z. Chen, R. Guo, G. Zou, H. Hou, W. Deng, X. Ji and J. Zhao, *Chem. Eng. J.*, 2020, 402.

[7] F. Tang, T. He, H. Zhang, X. Wu, Y. Li, F. Long, Y. Xiang, L. Zhu, J. Wu and X. Wu, *J. Electroanal. Chem.*, 2020, 873.

[8] Y. Fu, Q. Wei, G. Zhang, X. Wang, J. Zhang, Y. Hu, D. Wang, L. Zuin, T. Zhou, Y. Wu and S. Sun, *Adv. Energy Mater.*2018, 8, 1801445.

[9] G. Ren, Z. Luo, Y. Duan, X. Liu, Z. Yuan and F. Cai, *J. Alloy Compd.*, 2022, 898.

[10] T. H. Wu, L. H. Yen and Y. Q. Lin, *J. Colloid Interface Sci.*, 2022, 625, 354-362.

[11] Z. Deng, J. Huang, J. Liu, L. Ren, L. Zhu, X. Xiao and M. Tan, *Mater. Lett.*, 2019, 248, 207-210.

[12] A. Huang, W. Zhou, A. Wang, M. Chen, Q. Tian and J. Chen, *J. Energy Chem.*, 2021, 54, 475-481.

[13] T. Niu, J. Li, Y. Qi, X. Huang and Y. Ren, *J. Mater. Sci.*, 2021, 56, 16582-16590.

[14] S. Islam, M. H. Alfaruqi, V. Mathew, J. Song, S. Kim, S. Kim, J. Jo, J. P. Baboo, D. T. Pham, D. Y. Putro, Y.-K. Sun and J. Kim, *J. Mater. Chem. A*, 2017, 5, 23299-23309.

[15] H. Tang, W. Chen, N. Li, Z. Hu, L. Xiao, Y. Xie, L. Xi, L. Ni and Y. Zhu, *Energy Storage Mater.*, 2022, 48, 335-343.

[16] R. Zhang, P. Liang, H. Yang, H. Min, M. Niu, S. Jin, Y. Jiang, Z. Pan, J. Yan, X. Shen and J. Wang, *Chem. Eng. J.*, 2022, 433.

[17] J. Xie, G. Liu, K. Wang, X. Li, Y. Bai, S. Gao, L. Fan and R. Zheng, *Front. Chem. Sci. Eng.*, 2023, 17, 217-225.

[18] Y. Cai, R. Chua, S. Huang, H. Ren and M. Srinivasan, *Chem. Eng. J.*, 2020, 396.

[19] F. Kataoka, T. Ishida, K. Nagita, V. Kumbhar, K. Yamabuki and M. Nakayama, *ACS Appl. Energy Mater.* 2020, 3, 5, 4720-4726.

[20] B. Wu, G. Zhang, M. Yan, T. Xiong, P. He, L. He, X. Xu and L. Mai, *Small*, 2018, 14, e1703850.